ACS NANO

Open Access

This article is licensed under CC-BY-NC-ND 4.0

www.acsnano.org

Unexpected 4 × 4 Charge Density Wave in 1*H*-$NbTe_2$ Monolayer

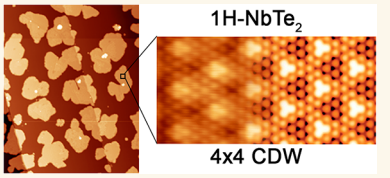
Noor ul Ain, Alireza Amiri, Fabian Calleja, Beatriz Muñiz Cano, Archit Dhingra, Riccardo Rurali, Amadeo L. Vázquez de Parga, Rodolfo Miranda, Miguel A. Valbuena, Enric Canadell, Jose Angel Silva-Guillén,* and Manuela Garnica*

Cite This: *ACS Nano* 2026, 20, 27706–27715

Read Online

ACCESS | Metrics & More | Article Recommendations | Supporting Information

ABSTRACT: **Transition metal ditellurides exhibit structural and electronic properties distinct from their selenide and sulfide counterparts, including the stabilization of multiple charge density wave (CDW) phases. Within the niobium compound family, notable differences in structure are also observed: bulk $NbTe_2$ crystallizes in the 1*T* phase, distinguishing it from $NbSe_2$ and NbS_2, which typically adopt both the 2*H* and 1*T* structures. However, in this work, we report the unexpectedly successful synthesis of two-dimensional (2D) islands of the metastable 1*H*-$NbTe_2$ phase via molecular beam epitaxy on epitaxial graphene supported on Ir(111). The phase is identified by its characteristic hexagonal lattice in combination with distinct spectroscopic features and the presence of mirror twin boundaries. A comprehensive analysis combining scanning tunneling spectroscopy (STS), angle-resolved photoemission spectroscopy (ARPES), and density functional theory (DFT) calculations confirms the metallic character and structural stability of the 1*H*-$NbTe_2$ phase. Furthermore, low-temperature STS measurements reveal the formation of a 4 × 4 CDW modulation, which is explained based on a phonon instability. These findings motivate the exploration of the complex phase behavior and electronic properties of $NbTe_2$ in the 2D limit.**



KEYWORDS: *Transition metal dichalcogenides, tellurides, charge density wave, molecular beam epitaxy, scanning tunneling microscopy, angle-resolved photoemission spectroscopy, density functional theory*

INTRODUCTION

Transition metal dichalcogenides (TMDs) have played a pivotal role in the development of modern low-dimensional physics. The experimental realization of charge density wave (CDW) states and the observation of nonlinear conductivity in some of these materials[1,2] sparked tremendous theoretical and experimental efforts. Groups IV and V TMDs[3,4] along with the Krogmann salts,[5] the blue bronze,[6] $NbSe_3$[7] and molecular conductors and superconductors of the TTF family,[8] provided some of the first experimental platforms to observe the new phenomena theoretically predicted by Peierls[9] and Fröhlich[10] for low-dimensional conductors.[11−13] However, groups IV and V TMDs soon came to be regarded as a distinct class among low-dimensional materials.[14] While the novel phenomena observed in many of the aforementioned systems could be largely explained within Fermi surface-based frameworks (i.e., weak-coupling approaches), this was not the case for group IV and V TMDs. Instead, their behavior appeared to be more accurately described by strong-coupling scenarios. The need to understand the competition between commensurate and incommensurate CDWs, superconductivity, Mott insulating phases, possible excitonic insulators, etc. in TMDs has fueled ongoing debate for over 40 years.[15,16]

Within the family of group V TMDs, the ditellurides have been demonstrated to behave in a remarkably different manner from their disulfide and diselenide counterparts. For example, bulk $NbTe_2$ only occurs as the 1*T* polymorph, where the transition metal atom is octahedrally coordinated by the chalcogen atoms, whereas its corresponding sulfide and selenide—such as NbS_2 and $NbSe_2$—occur also as the 2*H* polymorph, where the coordination of the transition metal atom (M) is trigonal prismatic.[17] Another peculiarity is that they exhibit a structure containing double zigzag chains in the M sublattice and they also show significant differences in their transport properties. For instance, bulk 1*T*-$NbTe_2$ exhibits the coexistence of a 3 × 1 CDW and superconductivity with a critical temperature of T_c = 0.5−0.74 K, whereas NbS_2 and $NbSe_2$ in the 2*H* phase show a single 3 × 3 CDW (latent in bulk) along with superconductivity at higher critical temper-

Received: April 15, 2026
Revised: July 30, 2026
Accepted: July 30, 2026
Published: October 2, 2026



ACS Publications

© 2026 The Authors. Published by American Chemical Society

Downloaded from pubs.acs.org/ancac3/article-pdf/20/41/27706/6873818/acsnano.6c07014.pdf by UNIV AUTONOMA DE MADRID user on 29 October 2026

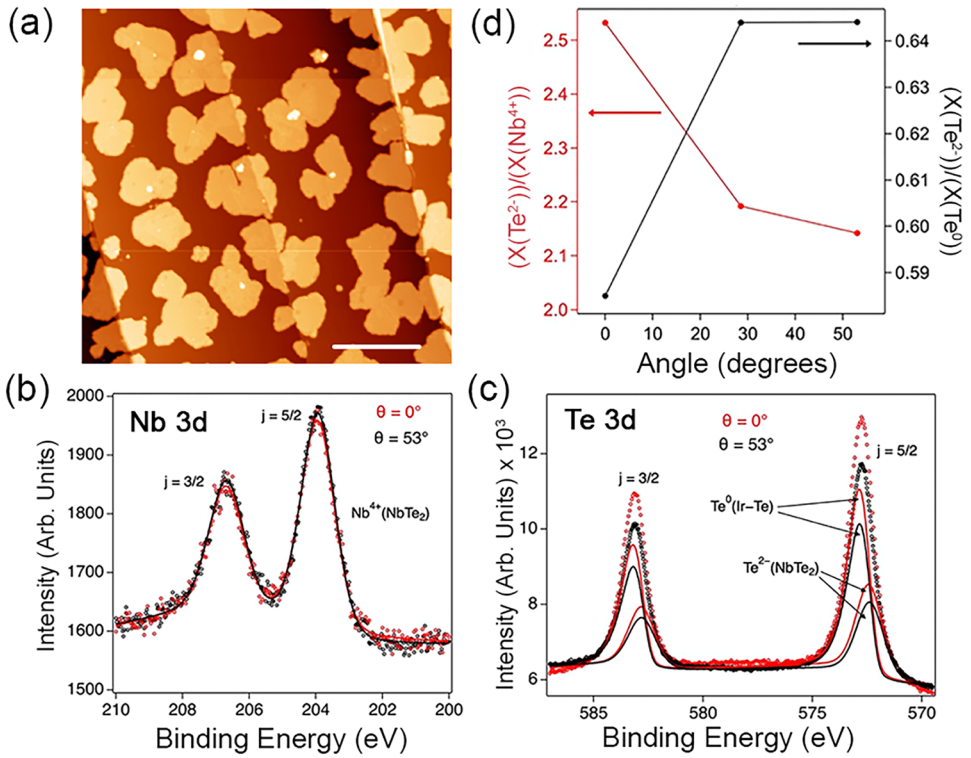


Figure 1. (a) Large STM image where 55% of the sample is covered with $NbTe_2$ islands (V_b = 1 V and I_t = 0.1 nA, 4.2 K, scale bar 40 nm). Photoemission spectra of the (b) Nb 3d (c) Te 3d core levels of $NbTe_2$. The spectra were recorded at photoemission takeoff angles between 0° (i.e., normal emission, shown in red) and 53° (i.e., grazing incidence, shown in black). (d) Ratio of the concentration of Te^{2-} to the concentration of Nb^{4+} (red curve) and ratio of the concentration of Te^{2-} to the concentration of Te^0 (black curve), as a function of the takeoff angle.

atures. These collective electronic properties and its competition have been the object of study since the late 60s.[18−25]

A major breakthrough in this area came with the ability to isolate layered materials as monolayers or few-layer structures, where two-dimensional (2D) physics could fully manifest.[16,26] Similar to the bulk at the monolayer limit, $NbSe_2$ and NbS_2 predominantly stabilize in the 1*H* phase, exhibiting a single 3 × 3 CDW together with superconductivity.[27,28] Recent studies have also demonstrated that the 1*T* monolayer phase of $NbSe_2$ can be stabilized by MBE growth, showing a $\sqrt{13} \times \sqrt{13}$ David-star reconstruction.[29] In stark contrast, 2D ditellurides such as VTe_2,[30] $NbTe_2$,[31−33] and $TaTe_2$[34−37] present multiple competing CDW configurations, offering a vast landscape to explore CDW physics. Although these findings were initially surprising, they are not difficult to rationalize. Because of the very diffuse orbitals of the Te atoms, there is a substantial overlap between the top of the tellurium-based valence bands and the bottom of the transition metal-based conduction bands. Such overlap is thus associated with a Te to M electron transfer.[38] The main factor contributing to the stabilization of the lattice under the CDW modulation is the additional metal−metal bonding provided by the metal−metal clustering, so that this electron transfer has a strong control on the nature of the adopted CDW.[39] Very recently, the close connection between tellurium to M electron transfer and the control of the structural landscape has been considered in detail for $TaTe_2$ monolayers.[35,37] Therefore, group V ditellurides hold a great promise as a very versatile platform for studying the CDW modulation and are thus attracting a strong attention.

At the 2D regime, $NbTe_2$ monolayer has been the most elusive of the Nb compounds.[27,40] Only recently, epitaxial growth of monolayer $NbTe_2$ has been achieved using graphene/SiC as a substrate. Tuning the growth condition, in particular the growth temperature, multiple CDW phases of its octahedral (1*T*) structure have been engineered.[33] In this context, the recent theoretical work by Jin *et al.* provides an alternative interpretation for several of the experimentally observed CDWs, proposing that different phases (1*T*/1H) may coexist in monolayer $NbTe_2$ and give rise to distinct CDW patterns.[41] Surprisingly, at high growth temperatures, a metallic $\sqrt{19} \times \sqrt{19}$ CDW, with an unusual star of David (SoD) lattice distortion, has been reported in contrast to the Mott insulating phase of its counterpart, 1*T*-$NbSe_2$ monolayer.[32]

Here, we report the first successful growth of the unstable 1*H*-$NbTe_2$ phase on epitaxial graphene on Ir(111) (gr/Ir(111)). We unequivocally identify this phase based on a combination of scanning tunneling microscopy (STM), angle-resolved photoemission spectroscopy (ARPES) and first-principles calculations. By analyzing the topographic images, we find an hexagonal lattice and the presence of mirror twin boundaries (MTBs) which have not been reported for 1*T* phases. At low temperatures, STS provides evidence of a 4 × 4 CDW accompanied by the opening of a pseudogap. The comparison of the obtained topographic images with simulations give a clear evidence that the 1*H* phase is that present in our samples. Our calculations also allow for a comprehensive understanding of the stability and formation of the CDW as well as its metallic properties. Moreover, the spectroscopic features align well with the band structure

https://doi.org/10.1021/acsnano.6c07014
ACS Nano 2026, 20, 27706−27715

Downloaded from pubs.acs.org/ancac3/article-pdf/20/41/27706/6873818/acsnano.6c07014.pdf by UNIV AUTONOMA DE MADRID user on 29 October 2026

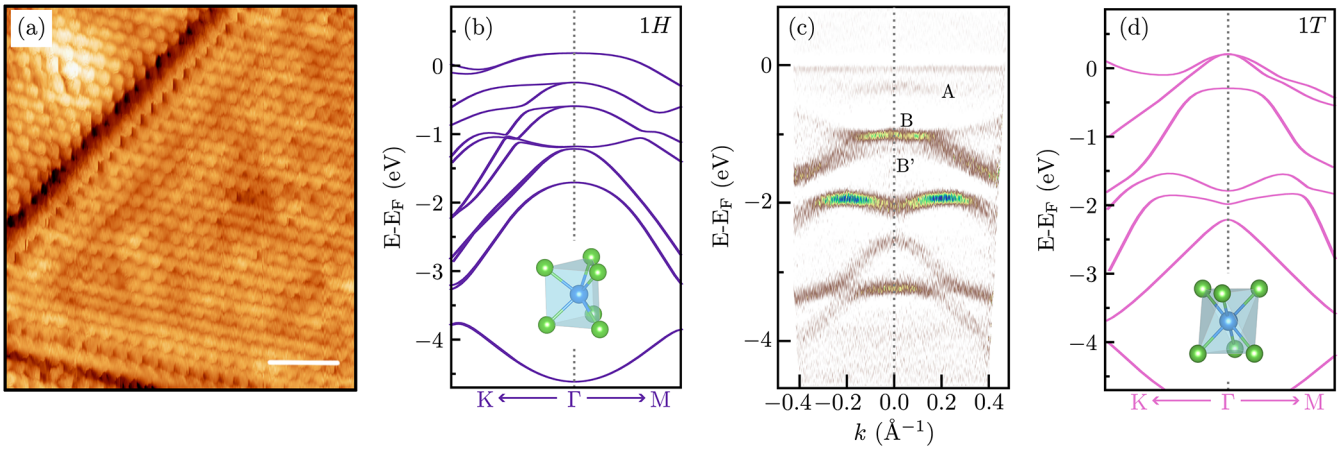


Figure 2. Direct comparison between ARPES curvature maps and DFT band structures of monolayer $NbTe_2$. (a) High resolution STM image of an island of $NbTe_2$ (V_b = 100 mV and I_t = 0.3 nA, 77 K, scale bar 1 nm). (b) DFT band structure with SOC along the *K*−Γ−*M* directions for the 1*H* structure, showing a similar *k*-point range as in the ARPES measurements. Inset: the corresponding crystal structure. (c) ARPES curvature map showing the electronic states A and B analyzed in the text. (d) DFT band structure with SOC along the *K*−Γ−*M* directions for the 1*T* structure, showing a similar *k*-point range as in the ARPES measurements. Inset: the corresponding crystal structure. The calculated band structures must be rigidly shifted by ∼−300 meV to match the experimental measurements, consistent with the charge transfer expected from Te intercalation (see Figure S21).

obtained from ARPES, which matches better with that of the calculated 1*H* structure than with that of the 1*T* one.

RESULTS

The deposition of Nb and Te on a gr/Ir(111) substrate at relative low temperatures (T = 423 K) results in well-defined islands, see Figure 1(a). To get a clearer picture of the surface of our sample, the angular dependence of the XPS spectra at room temperature (RT) was investigated by changing the photoemission angle between 0−53° with respect to the surface normal. According to the Beer−Lambert law, the detected photoelectron intensity decreases with increasing angle, making measurements at higher angles more sensitive to surface atoms. This approach allows us to unambiguously determine which atomic species populate the surface versus the bulk of the sample. The photoemission spectra of the Nb 3d core-level (shown in Figure 1(b)) reveal the existence of Nb in 4^+ oxidation state, whereas the Te 3d core-level spectra (in Figure 1(c)) show clear signatures of the presence of metallic Te in addition to the expected Te^{2-} 3d doublet (at lower binding energy), Figure 1(c). In agreement with the existing literature,[42] the Te 3d doublet appearing at the higher binding energy is attributed to the formation of an Ir−Te intermetallic alloy. Although the formation of such an intermetallic alloy was not expected a priori, it does not come off as a total surprise given that Te does intercalate during the growth of such systems.[43] To gain further physical insights into the surface structure of this system, angle-dependent changes in the Nb 3d and Te 3d core-level spectra were monitored. Variations in the ratio of concentration of Te^{2-} to that of Nb^{4+} and ratio of concentration of Te^{2-} to that of Te^0, as a function of photoemission takeoff angle, are plotted in Figure 1(d). The red curve in this figure clearly demonstrates that the surface of this system is dominated by Nb, and the black curve indicates that Te^{2-} is closer to the surface than Te^0, consistent with the fact that Te intercalation can result in the formation of an Ir−Te intermetallic alloy.

High-resolution STM images acquired at 77 K from the islands shown in Figure 1(a) reveal the presence of a hexagonal lattice with a periodicity of 3.77 ± 0.04 Å, together with the appearance of MTBs, as shown in Figure 2(a). MTBs are a natural consequence of the coalescence of two mirror grains with a misalignment of the atomic lattices by 60°, commonly observed in 1*H*-TMDs[44] and recently reported in electrochemical exfoliated 1*H*-$NbTe_2$ flakes by atomic-resolution scanning transmission electron microscopy (STEM).[45] The 1*T* phase, on the other hand, possesses an octahedral coordination with D_{3d} symmetry and an intrinsic center of inversion. Because of this centrosymmetry, mirror-related domains are crystallographically equivalent, and thus the formation of MTBs is not expected or energetically favorable. In 1*T* phases, a hexagonal crystal structure with 60° rotational domains corresponds to equivalent orientations of the same structure rather than distinct mirror domains. The observation of a hexagonal lattice, together with the appearance of MTBs, therefore points to the conclusion that the observed structure corresponds to the 1H-$NbTe_2$ phase.

As a second step in trying to put into a firm basis the 1*H* vs 1*T* nature of our samples we carried out ARPES measurements. The distinction between the two electronic structures is certainly a subtle one. A careful density functional theory (DFT) study of the electronic structure of both $NbTe_2$ and $TaTe_2$ showed a clear distinction (see Figures S9 and S13 of the SM and the work by Feng and co-workers[36]): while in the 1*H* case the first and second sets of bands at Γ are nondegenerate and degenerate, respectively, the opposite situation holds for the 1*T* structure (see Figures S8 and S9 of the SM). This holds even in the case of the calculation with SOC close to the center of the Brillouin zone, Γ, which is the region explored by our ARPES measurements. In the 1*H* form the Te atoms of one of the two sublayers lie just above those of the other Te sublayer and this simple structural difference leads to weaker Te···Te repulsions. Consequently, the upper Te-based band is more strongly raised and crosses the lower nondegenerate Nb-based band for the 1*T* form but not for the 1*H* one.

Thus, there is a key feature of the band structure near the Γ point allowing to distinguish between the two forms. Our RT

https://doi.org/10.1021/acsnano.6c07014
ACS Nano 2026, 20, 27706−27715

Downloaded from pubs.acs.org/ancac3/article-pdf/20/41/27706/6873818/acsnano.6c07014.pdf by UNIV AUTONOMA DE MADRID user on 29 October 2026

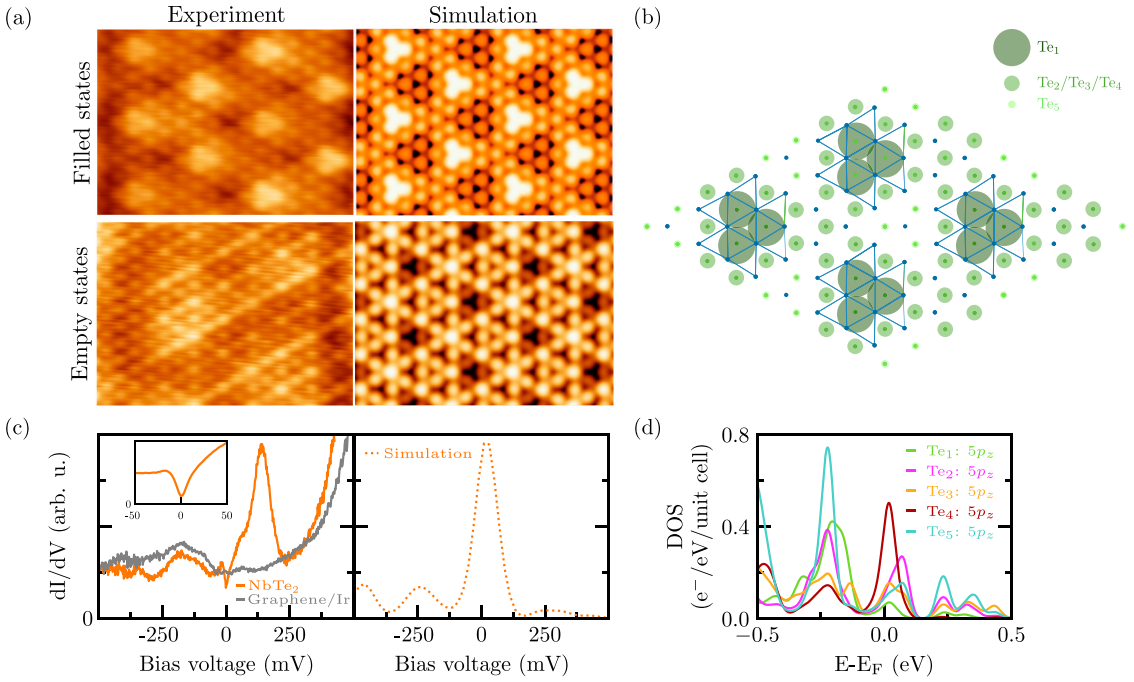


Figure 3. (a) Comparative of the experimental and calculated STM images for filled (V_b = −0.2 V) and empty (V_b = 0.2 V) states. (b) Schematic STM image for filled states, were the size of every circle is roughly proportional to the height of the Te atom. (c) Left panel: Measured STS on a 1*H*-(4 × 4) island (orange) and graphene/Ir (gray). Inset: CDW pseudogap of the $NbTe_2$. Right panel: Calculated STS on top of a Te. (d) Calculated projected DOS of the p_z orbitals for the different Te atoms.

ARPES spectra are shown in Figure 2, where we observe that band A is nondegenerate, while band B splits into two branches (B and B'), indicating a lifted degeneracy. This also agrees with the $TaTe_2$ ARPES measurements reported by Feng *et al.*[36]

Note that, to establish a direct correspondence between the ARPES spectra and the DFT calculations, it is necessary to consider that our $NbTe_2$ samples are grown on a Gr/Ir(111) substrate. Due to the growth conditions, Te atoms naturally intercalate between graphene and Ir(111), modifying the electronic environment of the heterostructure. As shown in Section 6 (Figure S20) of the Supporting Information (SI), the graphene Dirac cone is observed to be n-doped, with the Dirac point located ∼205 meV below the Fermi energy (E_F). Since pristine graphene on Ir(111) is typically p-doped, with the Dirac point lying ∼100 meV above E_F,[46] this corresponds to an overall energy shift of ∼300 meV. This experimentally determined value reflects the global charge redistribution in the system and provides a physically motivated upper bound for substrate-induced charge transfer effects. The DFT band structure, which does not include substrate interactions, should be therefore rigidly shifted by ∼300 meV to enable a meaningful comparison with the ARPES data. With this shift, the agreement between experiment and theory improves, particularly regarding the curvature and effective mass of the bands and supporting the assignment of the 1*H* phase as the structure present in our samples. The remaining discrepancies can be attributed to the simplified free-standing model used in the calculations, as well as to possible modifications of the lattice parameters and interlayer distances associated with Te and interface effects. A detailed analysis of these factors is beyond the scope of the present work.

In addition, we found in our DFT calculations that the ideal 1*H*-$NbTe_2$ monolayer was slightly more stable than 1*T*-$NbTe_2$ by 4.5 meV per formula unit (f.u.) with a Nb−Nb distance of 3.648 Å. The stability of the different structures does not change when adding SOC to the calculation (see Section 4.5 of the SI).

All in all, the finding of MTB, the features found in the ARPES measurements at RT and the energetics point toward the identification of the 1*H* phase as the one present in our grown $NbTe_2$ islands.

We then acquired high-resolution images at low temperature and in a region free of Te intercalation, such as Figure 3(a), that reveal the emergence of a 4 × 4 superstructure together with the hexagonal lattice previously observed at 77 K.

As we will see in the following, we are able to attribute this structure to the formation of a 4 × 4 CDW of the 1*H*-$NbTe_2$ phase unequivocally, in contradiction to the experimental data reported by Bai and co-workers,[33] which assigned this phase to the 4 × 4 1*T*-$NbTe_2$. This provides compelling evidence for the identification of the 1*H* phase in our samples.

The experimental and calculated STM images for filled (−0.2 V) and empty (+0.2 V) states are shown in Figure 3(a). The calculated images for opposite bias voltages are clearly different and exhibit the new periodicity. Importantly, they are consistent with the experimental results obtained for the same bias voltages. The results may be rationalized on the basis of the structural (height of the Te atoms) and electronic (i.e., partial Density of States (PDOS) at the tip) features of the 4 × 4 CDW of Figure 4(a). The atomic orbitals governing the shape of the STM images are the p_z orbitals of the upper Te atoms which are thus pointing outside the layer. There are five different types of Te atoms in the 4 × 4 CDW (see Te_1 to Te_5 in Figure 4(a)). However, in terms of their height, the different Te atoms can be sorted into three groups. The three Te atoms at the center of the cluster (Te_1, z = 1.97 Å) lie higher. Next, there is a group of three deeper-lying Te atoms (Te_2, Te_3, and

Downloaded from pubs.acs.org/ancac3/article-pdf/20/41/27706/6873818/acsnano.6c07014.pdf by UNIV AUTONOMA DE MADRID user on 29 October 2026

https://doi.org/10.1021/acsnano.6c07014
ACS Nano 2026, 20, 27706−27715

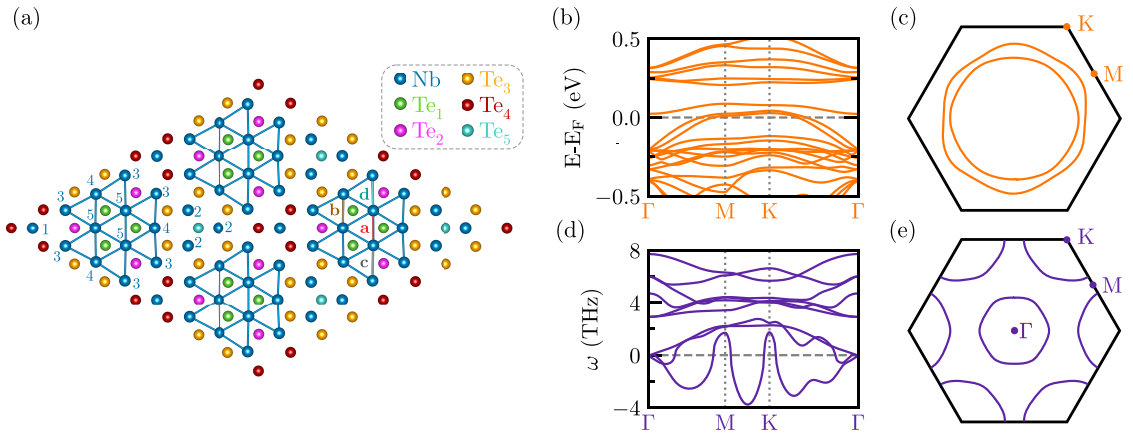


Figure 4. Crystal structure [Nb−Nb distances: a = 3.54 Å (red bonds), b = 3.43 Å (brown bonds), c = 3.48 Å (gray bonds), d = 3.53 Å (cyan bonds)] (a). Note that the different Nb and Te atoms are labeled with numbers and colors, respectively. Band structure (b) and Fermi surface (c) for the 1*H*-(4 × 4) structure. Phonon band structure (d) and Fermi surface (e) for the 1*H* undistorted structure.

Te_4, z = 1.87−1.89 Å). Finally, the Te_5 atoms are located even deeper (z = 1.78 Å). Simply taking into account these observations, a qualitative STM image for slightly negative biases (i.e., the energy region where the Te lone pairs occur) can be generated (see Figure 3b). This qualitative image, where the size of every circle is roughly proportional to the height of the Te atom, contains an hexagonal lattice of groups of three very intense peaks due to the Te_1 atoms and another hexagonal lattice of three considerably less intense peaks in the holes of the former lattice due to the Te_5 atoms. The two lattices are separated by three lines of intermediate intense peaks due to the Te_2, Te_3 and Te_4 atoms. This qualitative picture exhibits the same pattern of the calculated and experimental images for a −0.2 V bias voltage (i.e., the filled states in Figure 3a). Thus, as expected, the image corresponding to the filled states reflects the corrugation of the upper Te layer induced by the 4 × 4 clustering of the Nb atoms. The good agreement between the calculated and experimental images provides firm support for the nature of the modulation suggested by the DFT study (Figure 4a).

For a positive bias voltage of +0.2 V (empty states in Figure 3a) both the calculated and experimental images have changed. The three lines due to the Te_2, Te_3, and Te_4 atoms are now the more visible features. These three lines, mutually rotated by 60°, intersect at the position of the Te_4 atoms, which is associated with the more intense peak. To understand the change in the image when going from negative (filled states) to positive (empty states) bias voltages, we need to consider the PDOS of the five different types of Te p_z orbitals, i.e., the contribution of the p_z orbital of each type of surface Te atom to the DOS (see Figure 3d). The more striking observation of this figure is the occurrence of an intense peak around 0.12 eV wide around the Fermi level. This means that when going from filled to empty states there is a strong increase of the contribution of the Te_4 p_z orbitals and consequently, this position will become very brilliant. In contrast, the contribution of the Te_1 p_z become the smallest so that their contribution to the empty states will considerably decrease and these positions will be less bright. These two features, a direct consequence of the Nb−Nb clustering and its effect in the tellurium sublattice, connect the filled and empty states images. This observation provides a simple rational for the variation of the DFT and experimental STM images when changing the sign of the bias voltage, thus providing additional support for the nature of the proposed 4 × 4 structural modulation.

The dI/dV spectrum measured on the 1*H*-$NbTe_2$ at 4.2 K reveals a pseudogap feature centered at the Fermi level, not observed at 77 K (see Figure S4). The pseudogap (Δ) width is around 12 ± 1 mV, as shown in the inset of Figure 3(c). We attribute it to the development of the 4 × 4 CDW. The simulated STS spectrum is shown and compared with the experimental one in Figure 3(c). Note that the calculation has been carried out for an isolated monolayer. This spectrum contains a strong peak centered at slightly positive values of the bias voltage with quite small contributions for more negative values. Essentially it is a somewhat shifted version (∼0.12 V) of the experimental one. The strong peak originates from the Te p_z content of the three bands just above the Fermi level in Figure 4b from which the Te_1 contribution is just a minor component, as expected from the STM analysis. As usual in DFT calculations,[47] the small but distinctive pseudogap at the Fermi level associated with the CDW formation is not seen.

It is important to note that the orbitals probed in the tunneling experiments are those having a non-negligible weight at the tip, which are mostly the Te p_z orbitals. However, these orbitals are not necessarily the major components of the bands in the energy range probed.[47] In the present case, the bands around the Fermi level are dominated by the Nb d contributions. As a matter of fact, these bands essentially originate from the folding of the half-filled band of the ideal 1*H* lattice when the BZ becomes 1/16-th smaller. As shown by the fatbands in Figure S6 of the SI, the half-filled band in 1*H*-$NbTe_2$ mostly originates for the Nb $d_{x^2-y^2}/d_{xy}$ and Nb d_z^2 orbitals. An intriguing feature of the band structure of the 4 × 4 CDW (Figure 4b) is the occurrence of a quite flat empty band very near the Fermi level. If this band could be slightly stabilized so as to cross the Fermi level, both delocalized and localized states would occur at the Fermi level and it is possible that interesting magnetic properties could be observed. The origin of this peculiar band can be understood on the basis of a fat band analysis for the 4 × 4 structure (Figure S7 in the SI and Nb numbering in Figure 4a). The major components of this band along the full BZ are the d_z^2 orbitals of the Nb_3 atoms. Since the d_z^2 orbitals point along the direction perpendicular to the Nb sublattice they are not effective in making Nb−Nb bonding and hence the band is quite flat. In contrast, the two

https://doi.org/10.1021/acsnano.6c07014
ACS Nano 2026, 20, 27706−27715

Downloaded from pubs.acs.org/ancac3/article-pdf/20/41/27706/6873818/acsnano.6c07014.pdf by UNIV AUTONOMA DE MADRID user on 29 October 2026

partially filled bands crossing the Fermi level although still have a substantial participation of the d_z^2 orbitals of the Nb_3 and Nb_2 atoms, they also have a substantial participation (in fact comparable for Nb_3) of the $d_{x^2-y^2}/d_{xy}$ orbitals of Nb_3 and Nb_2 which are responsible for the delocalization and ensure the band dispersion and metallic conductivity of the system. The Te p_z orbitals even if they have a small participation into these orbitals they point directly toward the tip and determine the STM and STS spectra through the deformation induced by the Nb clustering. Importantly, topographic simulations of 1*T*-type 4 × 4 $NbTe_2$ CDWs do not agree with the features found in the experimental measurements (see Section 4.7 of the SI). Therefore, we conclude that the phase present in our samples must be 1*H*.

DISCUSSION

We report the growth and observation of $NbTe_2$ monolayer islands in the 1*H* polytype that suffer a CDW transition to an unpredicted 4 × 4 structure, different from those reported for its analog 1*H*-$TaTe_2$, thus confirming that substituting Nb for Ta induces significant changes in the electronic and structural properties of tellurium-based TMDs.

The formation of an *H* phase, which is not expected from the bulk structure of $NbTe_2$, is evidenced by several key observations. First, ARPES measurements reveal weak band dispersion. At the Γ point, $NbTe_2$ exhibits a distinct hole-like feature, indicating significant modifications in the electronic band structure which matches with our DFT calculations. Furthermore, the features of the experimental bands clearly match with those of the 1*H* structure and not those found in the 1*T* calculation. Moreover, when analyzing the STM topographic images, we find that the material exhibits a hexagonal lattice and 1D defects, which we attribute to the presence of metallic MTBs features (see Figures 2 and S2 of SI). However, MTBs are absent in the 1*T* phase as a consequence of its centrosymmetric octahedral coordination, which does not support mirror-related domains required for MTB formation. These line defects act as unique structural features, which can have a significant impact in the electronic properties of the 2D TMD. In semiconducting TMD monolayers, MTBs exhibit metallic characteristics and introduce quantum confinement effects, leading to the emergence of Tomonaga-Luttinger liquid behavior.[48−50] However, in the case of $NbTe_2$, STS measurements reveal no distinctive features associated with the MTBs (see Figure S2 of the SI). This suggests that the electronic properties of $NbTe_2$ are predominantly governed by its metallic nature and the formation of the CDW, with the MTBs acting as passive metallic defects that lack the capacity to host unconventional quantum phenomena. The absence of unique electronic states at the MTBs highlights a stark contrast with other 1*H*-TMDs,[48−50] emphasizing the role of material-specific interactions in determining the impact of such defects.

Additionally, at low temperatures we find a 4 × 4 reconstruction of the crystalline structure in the STM images and an opening of a pseudogap is revealed in the STS measurements at 4 K. Our calculations reveal a larger stabilization of the 4 × 4 modulation compared to the others explored (see below). Therefore, the combination of structural and electronic differences suggest the stabilization of a 4 × 4 CDW in the 1*H* phase. Note that this structure is different from that proposed by Jin and co-workers[41] which is quite asymmetric from a structural point of view. This is not the case of the present 4 × 4 CDW, which is simply the result of three tetramerizations along the main directions of the hexagonal lattice in order to optimize the metal−metal bonding, in the same way as the more stable 3 × 3 CDW of the 1*T*-$TaTe_2$ lattice is the result of three trimerizations[37] or the 2 × 2 CDW of the 1*H*-$TaTe_2$[36] lattice is the result of three dimerizations. The present structure falls thus within a family of general $n \times n$ CDWs resulting from three *n*-merizations along the main directions of the hexagonal lattice which, according to the present information, is a common modulation in MTe_2 group V transition metal ditellurides.

Figure 4(a) shows the 4 × 4 CDW structure as given by the DFT study. This structure is different from the several 4 × 4 CDWs and 3 × 3 CDW phases reported previously for its counterpart compounds 1*T*-$TaTe_2$[37] and 1*T*-$NbTe_2$ (see Section 4.9 in the SI). These differences can be attributed to the underlying lattice symmetry and connectivity of the transition metal coordination environments. In particular, the 1*T* and 1*H* polymorphs exhibit different structural frameworks: in the 1*T* structure, the transition metal atoms are located at the center of edge-sharing octahedra, whereas in the 1*H* structure, the octahedra are face-sharing. This distinction has important consequences for the lattice dynamics. The face-sharing geometry in the 1*H* phase imposes significantly more rigid structural constraints on the transition metal atoms compared to the 1*T* phase, thereby limiting the range of accessible CDW distortions. Consequently, the CDW instabilities of the 1*T* lattices usually provide a larger stabilization thus occurring at higher temperatures and are structurally different from those of the H-type polymorphs.

In our calculations, we also located a $\sqrt{19} \times \sqrt{19}$ phase containing triangular Nb_3 clusters although slightly different (see Figure S5 in the SI) from that in 1*H*-$TaTe_2$;[36] see Figure S18 in the SI. These results make clear the subtle differences between Nb and Ta ditellurides. We also located 3 × 3 CDWs similar to those reported for 1*H*-$NbSe_2$[51] (Figure S5) although they are less stable. The energies per f.u. of these phases relative to the ideal 1*H*-$NbTe_2$ monolayer are −24.7 meV (4 × 4), −16.2 meV (4 × 1), −15.0 meV (3 × 3) and −10.5 meV ($\sqrt{19} \times \sqrt{19}$). The energy difference between the 4 × 4 and 4 × 1 CDWs increases when doping with both holes and electrons. Interestingly, we were not able to find a 2 × 2 CDW as recently reported for 1*H*-$TaTe_2$ (see Figure S18 in the SI).[36] In summary, our calculations covered the more frequent types of supercells found in group V TMDs so that we tentatively conclude that the 4 × 4 CDW is the most stable for the 1*H*-$NbTe_2$. Therefore, our theoretical results are in good agreement with our experimental measurements.

As has long been discussed for the Nb and Ta disulfides and diselenides,[15] the modulation can be understood in terms of either a Fermi surface nesting mechanism or a phonon-based mechanism. The phonon dispersion and Fermi surface of the ideal 1*H*-$NbTe_2$ are shown in Figure 4(d,e), respectively. The Fermi surface contains rounded hexagons centered at Γ and K. Although there is some nesting due to the parallel sides of both intra or inter rounded hexagons, the nesting vectors are not in agreement with the occurrence of a commensurate 4 × 4 CDW so that the Fermi surface nesting mechanism can be dismissed. In the phonon dispersion, imaginary phonon modes with minima around 1/4 in the Γ-M line and a broad zone including the $(1/\sqrt{19},\ 1/\sqrt{19})$ point along Γ-K are identified. We thus

Downloaded from pubs.acs.org/ancac3/article-pdf/20/41/27706/6873818/acsnano.6c07014.pdf by UNIV AUTONOMA DE MADRID user on 29 October 2026

https://doi.org/10.1021/acsnano.6c07014
ACS Nano 2026, 20, 27706−27715

conclude that the 4 × 4 CDW most likely originates from a phonon instability.

Regarding the electronic properties, the 4 × 4 CDW is found to be metallic, exhibiting pseudocircular (i.e., strongly rounded hexagonal) Fermi surfaces (Figure 4(c)). The Nb−Nb distances within the 12 Nb cluster are calculated to be between 3.42 and 3.56 Å. This is a shortening of 0.228 and 0.098 Å with respect to the distance in the ideal 1*H* phase, i.e., a Nb−Nb shortening in between 6 and 2.7%, respectively. As expected, these shortenings are noticeably smaller than those found in experimental and theoretical studies (∼12%) of the 3 × 3 CDW in 1*T*-XTe_2 (X = Nb, Ta). As showed in a recent study of 1*T*-$TaTe_2$ CDWs,[37] a useful way to analyze the chemical origin of the stabilization afforded by the periodic lattice distortion is through the calculation of the so-called crystal orbital overlap populations (COOP).[52,53] Compared with the ideal 1*H*-$NbTe_2$, a large increase of +40% in the Nb−Nb overlap population per f.u. in the 4 × 4 CDW largely overrides the cost in Nb−Te bonding of −11.9%. In addition, the Te···Te interaction is also better in the distorted form (+7.4%). Clearly the optimization of the metal−metal bonding is the driving force of the modulation. Looking deeply into the structure there are both groups of three and single Nb atoms, clearly separated from the clusters by distances comparable or larger than in 1*H*-$NbTe_2$ (3.62−3.82 Å). The three Nb atoms in between the clusters are also left at distances (3.62 Å) similar to those of 1*H*-$NbTe_2$. Within the Nb 12-atom clusters, the *b* distances making the large triangle are the shorter, 3.43 Å, whereas the *a* distances forming the inner, smaller triangle are considerably larger, 3.54 Å (see colored bonds in Figure 4a). The large triangle, is capped by pairs of triangles with distances *c* of 3.48 Å and *d* of 3.43−3.54 Å. The gain in overlap population per f. u. is completely dominated by the contribution of the cluster, 94.9%. Note that within the cluster the contributions of the *b*, *c* and *d* bonds are very similar, ∼30%. That of the inner *a* bonds is clearly smaller, 7.7%, even taking into account that there are only three bonds. To the best of our knowledge this type of clusters has not been observed in other TMDs.

As mentioned, the Te to transition metal electron transfer plays an important role in governing the kind of CDW adopted by 1*T*-type tellurium-based TMDs. A fat band analysis of the ideal 1*H*-$NbTe_2$ (Figure S6 in the SI) clearly shows that such electron transfer does not occur in 1*H*-$NbTe_2$ monolayer. The top of the Te bands does not cross the Fermi level so that the lowest Nb-based d band is half-filled. This is also the case in the 4 × 4 structure: the fat band analysis shows that the Te-based bands do not cross the Fermi level, and consequently there is no formal electron transfer. This is an important difference with the 1*T*-$NbTe_2$ (see Figure S8 in the SI) and 1*T*-$TaTe_2$[37] monolayers suggesting that the Te···Te interactions are weaker in the 1*H* structure. However, note that the top of the Te band (occurring at M, see Figure S6 in the SI) is not very far from the Fermi level, and thus it can not be discarded that when the Te···Te interactions increase, as for instance in bilayers, trilayers or bulk, or under a small compression, the Te to M electron transfer can occur.

In bulk, the CDW transition temperature (T_{CDW}) is closely tied to structural distortions. The 1*H* phase resists distortion more than the 1*T* phase, likely due to differences in metal coordination and resulting, in general, in consistently lower CDW transition temperatures. Our findings suggest that the emergence of the 1*H* phase introduces fundamental changes in both lattice symmetry and electronic behavior, providing new insights into the phase stability and electronic correlations in $NbTe_2$.

CONCLUSIONS

The combination of STM/STS, XPS, ARPES, and DFT calculations has allowed us to identify the growth of the unexpected 1*H* phase of $NbTe_2$. STM imaging reveals a hexagonal structure characterized by the presence of MTBs. The qualitative agreement between the electronic band structure obtained from ARPES and the DFT calculations supports the assignment of this metallic phase to the 1*H* structure.

Furthermore, low-temperature STM/STS measurements reveal the emergence of a stable (4 × 4) CDW. Our theoretical calculations explored the most common types of supercells observed in group V TMDs, and we tentatively conclude that the (4 × 4) CDW is the most stable configuration for monolayer 1*H*-$NbTe_2$, in excellent agreement with our experimental observations. Notably, this phase is not stable in bulk $NbTe_2$, highlighting the crucial role of interlayer interactions in determining the phases of TMDs and providing a foundation for future studies exploring how doping, strain, or boundary engineering may be leveraged to access correlated or topological phases in this material.

METHODS

$NbTe_2$ was grown by molecular beam epitaxy (MBE) on a gr/Ir(111) sample. The base pressure during the experiments was 2 × 10^{-10} mbar. First, the Ir(111) single crystal was cleaned by repeated cycles of Ar^+ sputtering and annealing at 1500 K. Subsequently, the graphene was synthesized by chemical vapor decomposition (CVD) of ethylene (33 L) with the Ir(111) substrate held at 1400 K. Then, $NbTe_2$ was grown by coevaporation of elemental Nb (99.9+% purity) and Te (99.999% purity) from an e-beam evaporator and Knudsen cell, respectively, while maintaining the substrate at 423 K.

STM images were recorded in constant current mode and the differential conductance (d*I*/d*V*) spectra were taken using a lock-in amplifier (f = 763.7 Hz) at 77 and 4.2 K. The images were processed using the WSxM[54] and Gwyddion software.

X-ray photoemission spectroscopy (XPS) and angle-resolved photoemission spectroscopy (ARPES) measurements were carried out at the Spin-ARPES Laboratory of IMDEA Nanociencia. XPS spectra were acquired using a nonmonochromatized Al Kα X-ray source (SPECS XR-50, $h\nu$ = 1486.6 eV) and a SPECS Phoibos 150 hemispherical analyzer, providing an overall energy resolution of approximately 1 eV under the experimental conditions. ARPES experiments were performed with an UVS300 He discharge lamp from SPECS ($h\nu$ = 21.2 eV), yielding a spot size of ∼ 500 μm on the sample. The samples, previously characterized by STM, were transferred to the ARPES chamber using a UHV suitcase, always kept at pressures below 1 × 10^{-8} mbar. The analysis chamber operated at room temperature (RT) with a base pressure better than 1 × 10^{-10} mbar. ARPES measurements were performed with angular acceptance of ±10° in Medium Angle Mode and ±15° in Wide Angle Mode, yielding an angular resolution better than 0.05° (0.002 $Å^{-1}$) and 0.075° (0.003 $Å^{-1}$), respectively, for short- and long-range energy maps. The total energy resolution for ARPES at RT was approximately 80 meV.

First-principles calculations were carried out using a numerical atomic orbitals approach to density functional theory (DFT),[55,56] which was developed for efficient calculations in large systems and implemented in the SIESTA code.[57,58] We have used the generalized gradient approximation (GGA) and, in particular, the functional of Perdew *et al.*[59] Only the valence electrons are considered in the calculation, with the core being replaced by norm-conserving scalar

Downloaded from pubs.acs.org/ancac3/article-pdf/20/41/27706/6873818/acsnano.6c07014.pdf by UNIV AUTONOMA DE MADRID user on 29 October 2026

https://doi.org/10.1021/acsnano.6c07014
ACS Nano 2026, 20, 27706−27715

relativistic pseudopotentials[60,61] factorized in the Kleinman-Bylander form.[62] The nonlinear core−valence exchange-correlation scheme[63] was used for all elements. We have used a split-valence double-ζ basis set including polarization functions.[64] The energy cutoff of the real space integration mesh was set to 500 Ry. To build the charge density and, from this, obtain the DFT total energy and atomic forces, the Brillouin zone (BZ) was sampled with the Monkhorst−Pack scheme[65] using optimized grids. For the Fermi surface (FS), density of states (DOS) and Crystal Orbital Overlap Population (COOP) calculations, a finer grid was used. The forces and energies do not change significantly with the finer grid, which confirms the appropriateness of the grid for the relaxation as well as for the energies comparison. We checked the possible influence of the spin−orbit coupling (SOC) by performing SOC calculations as implemented in SIESTA.[66] Except for the expected doubling and avoided crossings of some bands no major effects were detected. In particular, we checked that none of the specifically reported results would be affected by its explicit inclusion. The details and results of these calculations are listed in the Supporting Information. For each structure, we optimized the lattice vectors as well as the atomic positions with a threshold of 0.01 eV/Å.

The 1*H* phonon band structure calculation was performed with phonopy[67,68] using a (11 × 11 × 1) supercell. The STM images were calculated using the Tersoff-Hamman aproximation and correspond to constant current images, i.e., they are a map of the heights producing a constant tip−surface current. They were plotted with WSxM. Most of the structures and Fermi surfaces were plotted using VESTA[69] and XCRYSDEN,[70] respectively.

■ ASSOCIATED CONTENT

Supporting Information

The Supporting Information is available free of charge at https://pubs.acs.org/doi/10.1021/acsnano.6c07014.

> Details on the growth of 1*H*-$NbTe_2$, details on the structure and spectroscopic charateristics of mirror twin boundaries, the evolution of the CDW with temperature, further DFT results such as other possible 1*H* structures, orbital weight analysis for the 1*H*-(1 × 1) and 1*H*-(4 × 4) structures, a comparison between the 1*H* and 1*T* band structures, the effect of spin−orbit coupling in the stability of the structures and the band structure, the $TaTe_2$ band structures, STM/STS simulations in 1*T*-4 × 4 structures, the cross-section view of the 1*H*-4 × 4 structure and alternative 1*T*-$NbTe_2$ and 1*H*-$TaTe_2$ structures as well as additional ARPES results, including raw data, curvature and second-derivative band maps, constant energy maps, and the full band dispersion from Γ to K_{Gr}, highlighting the graphene Dirac cone and its doping (PDF)

■ AUTHOR INFORMATION

Corresponding Authors

Jose Angel Silva-Guillén − *Instituto Madrileño de Estudios Avanzados en Nanociencia (IMDEA-Nanociencia), 28049 Madrid, Spain;* orcid.org/0000-0002-0483-5334; Email: joseangel.silva@imdea.org

Manuela Garnica − *Instituto Madrileño de Estudios Avanzados en Nanociencia (IMDEA-Nanociencia), 28049 Madrid, Spain; Instituto "Nicolás Cabrera", Universidad Autónoma de Madrid, 28049 Madrid, Spain;* orcid.org/0000-0002-7861-9490; Email: manuela.garnica@imdea.org

Authors

Noor ul Ain − *Instituto Madrileño de Estudios Avanzados en Nanociencia (IMDEA-Nanociencia), 28049 Madrid, Spain*

Alireza Amiri − *Instituto Madrileño de Estudios Avanzados en Nanociencia (IMDEA-Nanociencia), 28049 Madrid, Spain;* orcid.org/0009-0006-9274-143X

Fabian Calleja − *Instituto Madrileño de Estudios Avanzados en Nanociencia (IMDEA-Nanociencia), 28049 Madrid, Spain;* orcid.org/0000-0001-6007-8641

Beatriz Muñiz Cano − *Instituto Madrileño de Estudios Avanzados en Nanociencia (IMDEA-Nanociencia), 28049 Madrid, Spain*

Archit Dhingra − *Instituto Madrileño de Estudios Avanzados en Nanociencia (IMDEA-Nanociencia), 28049 Madrid, Spain;* Present Address: (A.D.) FinEstBeAMS Beamline, MAX IV-laboratoriet, Fotongatan 2, Lund, 22484, Sweden; orcid.org/0000-0001-9352-4361

Riccardo Rurali − *Institut de Ciència de Materials de Barcelona, ICMAB-CSIC, Bellaterra 08193, Spain;* orcid.org/0000-0002-4086-4191

Amadeo L. Vázquez de Parga − *Instituto Madrileño de Estudios Avanzados en Nanociencia (IMDEA-Nanociencia), 28049 Madrid, Spain; Instituto "Nicolás Cabrera", Universidad Autónoma de Madrid, 28049 Madrid, Spain; Departamento de Física de la Materia Condensada., Universidad Autónoma de Madrid, 28049 Madrid, Spain; Condensed Matter Physics Center (IFIMAC), Universidad Autónoma de Madrid (UAM), 28049 Madrid, Spain;* orcid.org/0000-0003-0551-1603

Rodolfo Miranda − *Instituto Madrileño de Estudios Avanzados en Nanociencia (IMDEA-Nanociencia), 28049 Madrid, Spain; Instituto "Nicolás Cabrera", Universidad Autónoma de Madrid, 28049 Madrid, Spain; Departamento de Física de la Materia Condensada., Universidad Autónoma de Madrid, 28049 Madrid, Spain; Condensed Matter Physics Center (IFIMAC), Universidad Autónoma de Madrid (UAM), 28049 Madrid, Spain*

Miguel A. Valbuena − *Instituto Madrileño de Estudios Avanzados en Nanociencia (IMDEA-Nanociencia), 28049 Madrid, Spain;* orcid.org/0000-0002-0585-5636

Enric Canadell − *Institut de Ciència de Materials de Barcelona, ICMAB-CSIC, Bellaterra 08193, Spain; Royal Academy of Sciences and Arts of Barcelona, Chemistry Section, 08002 Barcelona, Spain;* orcid.org/0000-0002-4663-5226

Complete contact information is available at: https://pubs.acs.org/10.1021/acsnano.6c07014

Notes

The authors declare no competing financial interest.

■ ACKNOWLEDGMENTS

The authors acknowledge support by the Spanish Ministerio de Ciencia e Innovacion (Grant no. PID2021-123776NB-C21, PID2021-128011NB-I00, and PID2024-157655NB-I00). IMDEA Nanociencia and IFIMAC acknowledge financial support from the Spanish Ministry of Science and Innovation "Severo Ochoa" (Grant CEX2020-001039-S and CEX2025-001660-S) and "María de Maeztu" (Grant CEX2023-001316-M) Programme for Centres of Excellence in R&D, respectively. Financial support through the (MAD2D-CM)-MRR MATERIALES AVANZADOS-IMDEA-NC and (MAD2D-CM)-

Downloaded from pubs.acs.org/ancac3/article-pdf/2041/27706/6873818/acsnano.6c07014.pdf by UNIV AUTONOMA DE MADRID user on 29 October 2026

MRR MATERALES AVANZADOS-UAM is acknowledged. M.G. has received financial support through the "Ramón y Cajal" Fellowship program (RYC2020-029317-I) and "Ayudas para Incentivar la Consolidación Investigadora" (CNS2022-135175). J.A. S.-G. has received financial support from NOVMOMAT, project PID2022-142162NB-I00 funded by MICIU/AEI/10.13039/501100011033 and by FEDER, UE, and the "Ramón y Cajal" Fellowship program, grant RYC2023-044383-I financed by MICIU/AEI/10.13039/501100011033 and FSE+. E.C. and R.R. were supported by the Spanish MCIN/AEI/10.13039/501100011033 and AEI through Grants PID2022-139776NB-C61 and PID2024-162811NB-I00, the Severo Ochoa Matrans42 (CEX2023-0001263-S) Excellence Centre distinction, as well as by Generalitat de Catalunya (Grant No. 2021 SGR 01519). We thankfully acknowledge RES resources provided by BSC in MareNostrum5 to FI-2024-3-0030, FI-2025-1-0039, FI-2025-2-0026, FI-2025-3-0035, and FI-2026-1-0068. M.A.V. acknowledges financial support from the Comunidad de Madrid through project TEC-2024/TEC-380 (Mag4TIC-CM) and from the M-ERANET GREEN-MEM project (PCI2025-163177) funded by AEI/MICIU through the International Collaboration Projects program.

REFERENCES

(1) Meerschaut, A.; Rouxel, J. *Crystal Chemistry and Properties of Materials with Quasi-One-Dimensional Structures*; Rouxel, J., Ed.; D. Reidel Publishing Company: Dordrecht, Holland, 1986; pp 205−279.
(2) Dumas, J.; Schlenker, C.; Marcus, J.; Buder, R. Nonlinear Conductivity and Noise in the Quasi One-Dimensional Blue Bronze $K_{0.30}MoO_3$. *Phys. Rev. Lett.* **1983**, *50*, 757−760.
(3) Wilson, J. A.; Di Salvo, F. J.; Mahajan, S. Charge-density waves and superlattices in the metallic layered transition metal dichalcogenides. *Adv. Phys.* **1975**, *24*, 117−201.
(4) Scruby, C. B.; Williams, P. M.; Parry, G. S. The role of charge density waves in structural transformations of 1T-TaS_2. *Philos. Mag.* **1975**, *31*, 255−274.
(5) Comès, R.; Lambert, M.; Launois, H.; Zeller, H. R. Evidence for a Peierls Distortion or a Kohn Anomaly in One-Dimensional Conductors of the Type $K_2Pt(CN)_4Br_{0.30}{\cdot}xH_20$. *Phys. Rev. B* **1973**, *8*, 571−575.
(6) *Low Dimensional Electronic Properties of Molybdenum Bronzes and Oxides*; Schlenker, C., Ed.; Physics and Chemistry of Materials with Low-Dimensional Structures; Springer: Netherlands, 1989.
(7) Monceau, P.; Ong, N. P.; Portis, A. M.; Meerschaut, A.; Rouxel, J. Electric Field Breakdown of Charge-Density-Wave-Induced Anomalies in $NbSe_3$. *Phys. Rev. Lett.* **1976**, *37*, 602−606.
(8) Jérome, D.; Schulz, H. J. Organic conductors and superconductors. *Adv. Phys.* **1982**, *31*, 299−490.
(9) Peierls, R. *Quantum Theory of Solids*; Oxford University Press, London, 1955.
(10) Fröhlich, H. On the Theory of Superconductivity: The One-Dimensional Case. *Proc. R. Soc. London, Ser. A* **1954**, *223*, 296−305.
(11) Monceau, P. Electronic crystals: an experimental overview. *Adv. Phys.* **2012**, *61*, 325−581.
(12) Pouget, J.-P.; Canadell, E. Structural Approach to Charge Density Waves in Low-Dimensional Systems: Electronic Instability and Chemical Bonding. *Rep. Prog. Phys.* **2024**, *87*, No. 026501.
(13) Grüner, G. The dynamics of charge density waves. *Rev. Mod. Phys.* **1988**, *60*, 1129−1181.
(14) McMillan, W. L. Microscopic model of charge-density waves in 2*H*-$TaSe_2$. *Phys. Rev. B* **1977**, *16*, 643−650.
(15) Rossnagel, K. On the origin of charge-density waves in select layered transition-metal chalcogenides. *J. Phys.: Condens. Matter* **2011**, *23*, No. 213001.
(16) Manzeli, S.; Ovchinnikov, D.; Pasquier, D.; Yazyev, O. Y.; Kis, A. 2D transition metal dichalcogenides. *Nat. Rev. Mater.* **2017**, *2*, No. 17033.
(17) Hulliger, F. *Structural Chemistry of Layer-Type Phases*; D. Reidel Publishing Company, Dordrecht, Holland, 1976.
(18) Nagata, S.; Abe, T.; Terashima, S.; Ishihara, Y.; Tsutsumi, K. Superconductivity in layered-structure compound $NbTe_2$. *Physica B* **1994**, *194−196*, 1981−1982.
(19) Van Maaren, M.; Schaeffer, G. M. Some new superconducting group V^a dichalcogenides. *Phys. Lett.* **1967**, *24*, 645−646.
(20) Wilson, J. A. Questions concerning the form taken by the charge-density wave and the accompanying periodic-structural distortions in 2*H*-$TaSe_2$, and closely related materials. *Phys. Rev. B* **1978**, *17*, 3880−3898.
(21) Vernes, A.; Ebert, H.; Bensch, W.; Heid, W.; Näther, C. Crystal structure, electrical properties and electronic band structure of tantalum ditelluride. *J. Phys.: Condens. Matter* **1998**, *10*, 761−774.
(22) Chen, H.; Li, Z.; Guo, L.; Chen, X. Anisotropic magneto-transport and magnetic properties of low-temperature phase of $TaTe_2$. *Europhys. Lett.* **2017**, *117*, No. 27009.
(23) Sörgel, T.; Nuss, J.; Wedig, U.; Kremer, R.; Jansen, M. A new low temperature modification of $TaTe_2$-Comparison to the room temperature and the hypothetical 1*T*-$TaTe_2$ modification. *Mater. Res. Bull.* **2006**, *41*, 987−1000.
(24) Liu, Y.; Lu, W. J.; Shao, D. F.; Zu, L.; Kan, X. C.; Song, W. H.; Sun, Y. P. Structural, electrical, and thermoelectric properties of distorted 1*T*-$Ta_{1-x}Nb_xTe_2$ single crystals. *Europhys. Lett.* **2015**, *109*, No. 17003.
(25) Li, S.; Dong, Q.; Feng, J.; Wang, Y.; Hou, M.; Deng, W.; Susilo, R. A.; Li, N.; Dong, H.; Wan, S.; Gao, C.; Chen, B. Evolution of Structural and Electronic Properties in $NbTe_2$ under High Pressure. *Inorg. Chem.* **2021**, *60*, 7857−7864.
(26) Chhowalla, M.; Shin, H. S.; Eda, G.; Li, L.-J.; Loh, K. P.; Zhang, H. The chemistry of two-dimensional layered transition metal dichalcogenide nanosheets. *Nat. Chem.* **2013**, *5*, 263−275.
(27) Ugeda, M. M.; Bradley, A. J.; Zhang, Y.; Onishi, S.; Chen, Y.; Ruan, W.; Ojeda-Aristizabal, C.; Ryu, H.; Edmonds, M. T.; Tsai, H.-Z.; Riss, A.; Mo, S.-K.; Lee, D.; Zettl, A.; Hussain, Z.; Shen, Z.-X.; Crommie, M. F. Characterization of collective ground states in single-layer $NbSe_2$. *Nat. Phys.* **2016**, *12*, 92−97.
(28) Knispel, T.; Berges, J.; Schobert, A.; van Loon, E. G. C. P.; Jolie, W.; Wehling, T.; Michely, T.; Fischer, J. Unconventional Charge-Density-Wave Gap in Monolayer NbS_2. *Nano Lett.* **2024**, *24*, 1045−1051.
(29) Zhang, Q.; He, W.-Y.; Zhang, Y.; Chen, Y.; Jia, L.; Hou, Y.; Ji, H.; Yang, H.; Zhang, T.; Liu, L.; Gao, H.-J.; Jung, T. A.; Wang, Y. Quantum spin liquid signatures in monolayer 1T-NbSe2. *Nat. Commun.* **2024**, *15*, No. 2336.
(30) Coelho, P. M.; Lasek, K.; Nguyen Cong, K.; Li, J.; Niu, W.; Liu, W.; Oleynik, I. I.; Batzill, M. Monolayer Modification of VTe_2 and Its Charge Density Wave. *J. Phys. Chem. Lett.* **2019**, *10*, 4987−4993.
(31) Zhang, K.; Zou, N.; Ren, Y.; Wu, J.; Si, C.; Duan, W. Realization of Coexisting Charge Density Wave and Quantum Spin/Anomalous Hall State in Monolayer $NbTe_2$. *Adv. Funct. Mater.* **2022**, *32*, No. 2111675.
(32) Taguchi, T.; Sugawara, K.; Oka, H.; Kawakami, T.; Saruta, Y.; Kato, T.; Nakayama, K.; Souma, S.; Takahashi, T.; Fukumura, T.; Sato, T. Charge order with unusual star-of-David lattice in monolayer $NbTe_2$. *Phys. Rev. B* **2023**, *107*, No. L041105.
(33) Bai, Y.; Jian, T.; Pan, Z.; Deng, J.; Lin, X.; Zhu, C.; Huo, D.; Cheng, Z.; Liu, Y.; Cui, P.; Zhang, Z.; Zou, Q.; Zhang, C. Realization of Multiple Charge-Density Waves in $NbTe_2$ at the Monolayer Limit. *Nano Lett.* **2023**, *23*, 2107−2113.
(34) Hwang, J.; Jin, Y.; Zhang, C.; Zhu, T.; Kim, K.; Zhong, Y.; Lee, J.-E.; Shen, Z.; Chen, Y.; Ruan, W.; Ryu, H.; Hwang, C.; Lee, J.; Crommie, M. F.; Mo, S.-K.; Shen, Z.-X. A Novel $\sqrt{19} \times \sqrt{19}$ Superstructure in Epitaxially Grown 1*T*-$TaTe_2$. *Adv. Mater.* **2022**, *34*, No. 2204579.

Downloaded from pubs.acs.org/ancac3/article-pdf/2041/27706/6873818/acsnano.6c07014.pdf by UNIV AUTONOMA DE MADRID user on 29 October 2026

https://doi.org/10.1021/acsnano.6c07014
ACS Nano 2026, 20, 27706−27715

(35) Di Bernardo, I.; Ripoll-Suau, J.; Silva-Guillén, J. A.; Calleja, F.; Ayani, C. G.; Miranda, R.; Canadell, E.; Garnica, M.; de Parga, A. M. V. Metastable Polymorphic Phases in Monolayer $TaTe_2$. *Small* **2023**, *19*, No. 2300262.
(36) Feng, R.; Wang, W.; Bao, C.; Zhang, Z.; Wang, F.; Zhang, H.; Yao, J.; Xu, Y.; Yu, P.; Ji, S.-H.; Si, C.; Zhou, S. Selective Control of Phases and Electronic Structures of Monolayer $TaTe_2$. *Adv. Mater.* **2024**, *36*, No. 2302297.
(37) Silva-Guillén, J. A.; Canadell, E. Rich structural, electronic, and bonding landscape of 1*T*-type $TaTe_2$ single layers. *Phys. Rev. B* **2025**, *111*, No. 064114.
(38) Canadell, E.; Jobic, S.; Brec, R.; Rouxel, J.; Whangbo, M.-H. Importance of short interlayer Te···Te contacts for the structural distortions and physical properties of CdI_2-type layered transition-metal ditellurides. *J. Solid State Chem.* **1992**, *99*, 189−199.
(39) Whangbo, M. H.; Canadell, E. Analogies between the concepts of molecular chemistry and solid-state physics concerning structural instabilities. Electronic origin of the structural modulations in layered transition metal dichalcogenides. *J. Am. Chem. Soc.* **1992**, *114*, 9587−9600.
(40) Stan, R. M.; Mahatha, S. K.; Bianchi, M.; Sanders, C. E.; Curcio, D.; Hofmann, P.; Miwa, J. A. Epitaxial single-layer NbS_2 on Au(111): Synthesis, structure, and electronic properties. *Phys. Rev. Mater.* **2019**, *3*, No. 044003.
(41) Jin, H.; Wei, T.; Huang, B. Incognizant 1*T*/1*H* Charge-Density-Wave Phases in Monolayer $NbTe_2$. *Nano Lett.* **2024**, *24*, 10892−10898.
(42) Jiang, B.; Xue, H.; Wang, P.; Du, H.; Kang, Y.; Zhao, J.; Wang, S.; Zhou, W.; Bian, Z.; Li, H.; Henzie, J.; Yamauchi, Y. Noble-Metal−Metalloid Alloy Architectures: Mesoporous Amorphous Iridium−Tellurium Alloy for Electrochemical N_2 Reduction. *J. Am. Chem. Soc.* **2023**, *145*, 6079−6086.
(43) Cano, B. M.; Calleja, F.; Pacilè, D.; Cuxart, M. G.; Pisarra, M.; Sindona, A.; Martín, F.; Salagre, E.; Segovia, P.; Michel, E. G.; de Parga, A. L. V.; Miranda, R.; Camarero, J.; Garnica, M.; Valbuena, M. A. Engineering a Spin-Orbit Bandgap in Graphene-Tellurium Heterostructures. *Adv. Funct. Mater.* **2025**, *35*, No. 2425154.
(44) Batzill, M. Mirror twin grain boundaries in molybdenum dichalcogenides. *J. Phys.: Condens. Matter* **2018**, *30*, No. 493001.
(45) Han, X.; You, J.-Y.; Han, Z.; Meng, Y.; Zhao, X. Geminal Mirror Twin Boundaries in H-Phase $NbTe_2$. *Nano Lett.* **2025**, *25*, 5843−5851.
(46) Pletikosić, I.; Kralj, M.; Pervan, P.; Brako, R.; Coraux, J.; N'Diaye, A. T.; Busse, C.; Michely, T. Dirac Cones and Minigaps for Graphene on Ir(111). *Phys. Rev. Lett.* **2009**, *102*, No. 056808.
(47) Silva-Guillén, J. n.; Ordejón, P.; Guinea, F.; Canadell, E. Electronic structure of 2*H*-$NbSe_2$ single-layers in the CDW state. *2D Mater.* **2016**, *3*, No. 035028.
(48) Jolie, W.; Murray, C.; Weiß, P. S.; Hall, J.; Portner, F.; Atodiresei, N.; Krasheninnikov, A. V.; Busse, C.; Komsa, H.-P.; Rosch, A.; Michely, T. Tomonaga-Luttinger Liquid in a Box: Electrons Confined within MoS_2 Mirror-Twin Boundaries. *Phys. Rev. X* **2019**, *9*, No. 011055.
(49) Xia, Y.; Zhang, J.; Jin, Y.; Ho, W.; Xu, H.; Xie, M. Charge Density Modulation and the Luttinger Liquid State in $MoSe_2$ Mirror Twin Boundaries. *ACS Nano* **2020**, *14*, 10716−10722.
(50) Zhu, T.; Ruan, W.; Wang, Y. Q.; Tsai, H. Z.; Wang, S.; Zhang, C.; Wang, T.; Liou, F.; Watanabe, K.; Taniguchi, T.; Neaton, J. B.; Weber-Bargioni, A.; Zettl, A.; Qiu, Z. Q.; Zhang, G.; Wang, F.; Moore, J. E.; Crommie, M. F. Imaging gate-tunable Tomonaga−Luttinger liquids in 1*H*-$MoSe_2$ mirror twin boundaries. *Nat. Mater.* **2022**, *21*, 748−753.
(51) Guster, B.; Rubio-Verdú, C.; Robles, R.; Zaldívar, J.; Dreher, P.; Pruneda, M.; Silva-Guillén, J. A.; Choi, D.-J.; Pascual, J. I.; Ugeda, M. M.; Ordejón, P.; Canadell, R. Coexistence of Elastic Modulations in the Charge Density Wave State of 2*H*-$NbSe_2$. *Nano Lett.* **2019**, *19*, 3027−3032.
(52) Hughbanks, T. R.; Hoffmann, R. Chains of trans-edge-sharing molybdenum octahedra: metal-metal bonding in extended systems. *J. Am. Chem. Soc.* **1983**, *105*, 3528−3537.
(53) Dronskowski, R. *Computational Chemistry of Solid State Materials: A Guide for Materials Scientists, Chemists, Physicists and Others*; Wiley-VCH Verlag GmbH & Co: Weinheim, 2005.
(54) Horcas, I.; Fernández, R.; Gómez-Rodríguez, J. M.; Colchero, J.; Gómez-Herrero, J.; Baro, A. M. WSXM: a software for scanning probe microscopy and a tool for nanotechnology. *Rev. Sci. Instrum.* **2007**, *78*, No. 013705.
(55) Kohn, W.; Sham, L. J. Self-Consistent Equations Including Exchange and Correlation Effects. *Phys. Rev.* **1965**, *140*, A1133−A1138.
(56) Hohenberg, P.; Kohn, W. Inhomogeneous Electron Gas. *Phys. Rev.* **1964**, *136*, B864−B871.
(57) Artacho, E.; Anglada, E.; Diéguez, O.; Gale, J. D.; García, A.; Junquera, J.; Martin, R. M.; Ordejón, P.; Pruneda, J. M.; Sánchez-Portal, D.; Soler, J. M. The Siesta method; developments and applicability. *J. Phys.: Condens. Matter* **2008**, *20*, No. 064208.
(58) Soler, J. M.; Artacho, E.; Gale, J. D.; García, A.; Junquera, J.; Ordejón, P.; Sánchez-Portal, D. The Siesta method for ab initio order-N materials simulation. *J. Phys.: Condens. Matter* **2002**, *14*, 2745−2779.
(59) Perdew, J. P.; Ruzsinszky, A.; Csonka, G. I.; Vydrov, O. A.; Scuseria, G. E.; Constantin, L. A.; Zhou, X.; Burke, K. Restoring the Density-Gradient Expansion for Exchange in Solids and Surfaces. *Phys. Rev. Lett.* **2008**, *100*, No. 136406.
(60) van Setten, M.; Giantomassi, M.; Bousquet, E.; Verstraete, M.; Hamann, D.; Gonze, X.; Rignanese, G.-M. The PseudoDojo: Training and grading a 85 element optimized norm-conserving pseudopotential table. *Comput. Phys. Commun.* **2018**, *226*, 39−54.
(61) García, A.; Verstraete, M. J.; Pouillon, Y.; Junquera, J. The psml format and library for norm-conserving pseudopotential data curation and interoperability. *Comput. Phys. Commun.* **2018**, *227*, 51−71.
(62) Kleinman, L.; Bylander, D. M. Efficacious Form for Model Pseudopotentials. *Phys. Rev. Lett.* **1982**, *48*, 1425−1428.
(63) Louie, S. G.; Froyen, S.; Cohen, M. L. Nonlinear ionic pseudopotentials in spin-density-functional calculations. *Phys. Rev. B* **1982**, *26*, 1738−1742.
(64) Artacho, E.; Sánchez-Portal, D.; Ordejón, P.; García, A.; Soler, J. M. Linear-Scaling ab-initio Calculations for Large and Complex Systems. *Phys. Stat. Solidi (b)* **1999**, *215*, 809−817.
(65) Monkhorst, H. J.; Pack, J. D. Special points for Brillouin-zone integrations. *Phys. Rev. B* **1976**, *13*, 5188−5192.
(66) Cuadrado, R.; Cerdá, J. I. Fully relativistic pseudopotential formalism under an atomic orbital basis: spin−orbit splittings and magnetic anisotropies. *J. Phys.: Condens. Matter* **2012**, *24*, No. 086005.
(67) Togo, A.; Chaput, L.; Tadano, T.; Tanaka, I. Implementation strategies in phonopy and phono3py. *J. Phys.: Condens. Matter* **2023**, *35*, No. 353001.
(68) Togo, A. First-principles Phonon Calculations with Phonopy and Phono3py. *J. Phys. Soc. Jpn.* **2023**, *92*, No. 012001.
(69) Momma, K.; Izumi, F. *VESTA3* for three-dimensional visualization of crystal, volumetric and morphology data. *J. Appl. Crystallogr.* **2011**, *44*, 1272−1276.
(70) Kokalj, A. XCrySDen—a new program for displaying crystalline structures and electron densities. *J. Mol. Graphics Modelling* **1999**, *17*, 176−179.

Downloaded from pubs.acs.org/ancac3/article-pdf/20/41/27706/6873818/acsnano.6c07014.pdf by UNIV AUTONOMA DE MADRID user on 29 October 2026

https://doi.org/10.1021/acsnano.6c07014
ACS Nano 2026, 20, 27706−27715